DOI: 10.1002/smll.201802086
Article Type: Full Paper

Rational Design Principles for the Transport and Subcellular Distribution of Nanomaterials into Plant Protoplasts

*Tedrick Thomas Salim Lew, Min Hao Wong, Seon-Yeong Kwak, Rosalie Sinclair, Volodymyr B. Koman, and Michael S. Strano**

T. T. S. Lew, M. H. Wong, Dr. S.Y. Kwak, R. Sinclair, Dr. V. B. Koman, Prof. M. S. Strano
Department of Chemical Engineering
Massachusetts Institute of Technology
Cambridge, MA 02139, USA
*Corresponding author's email address: strano@mit.edu

KEYWORDS: plant protoplasts; targeted delivery; zeta potential; single-walled carbon nanotubes; imaging flow cytometry.

ABSTRACT

The ability to control the subcellular localization of nanoparticles within living plants offers unique advantages for targeted biomolecule delivery and enables important applications in plant bioengineering. However, the mechanism of nanoparticle transport past plant biological membranes has been poorly understood. Here, we present a mechanistic study of nanoparticle cellular uptake into plant protoplasts. We advance an experimentally-validated mathematical model of lipid exchange envelope penetration mechanism for protoplasts, which predicts that the subcellular distribution of nanoparticles in plant cells is dictated by the particle size and the magnitude of the zeta potential. Our mechanism is completely generic, describing nanoparticles ranging from quantum dots, gold and silica nanoparticles, nanoceria and single-walled carbon nanotubes (SWNTs). In addition, we demonstrate the use of imaging flow cytometry to investigate the influence of protoplasts' morphological characteristics on nanoparticle uptake efficiency. Using DNA-wrapped SWNTs as model nanoparticles, we found that glycerolipids, the predominant lipids in chloroplast membranes, exhibit stronger lipid-nanoparticle interaction than phospholipids, the major constituent in protoplast membrane. Our work can guide the rational design of nanoparticles for targeted delivery into specific compartments within plant cells without the use of chemical or mechanical aid, potentially enabling various plant engineering applications and furthering our understanding of plant biology.

Introduction

The ability of nanoparticles to penetrate biological membranes has led to significant development in utilizing nanoparticles as biomolecular cargo nanocarriers in mammalian cells. For example, surface functionalized nanoparticles have been proven to be able to deliver DNA and small drug molecules into animal cells and tissues.[1–4] Recently, there has been much interest in the use of nanomaterials as delivery vehicles for biomolecules into plant cells, especially for plant genetic transformation.[5–7] Nanoparticle-based delivery methods have the potential of overcoming the current limitations in plant genome engineering, with unique advantages such as high throughput, low cytotoxicity and wide applicability to a range of plant species.[8,9] Furthermore, when bound to nanoparticles, biomolecular cargos are shielded from enzymatic degradation within biological environments[10,11] and can be potentially controlled to target specific organelles or tissues.[12] However, the incorporation of nanomaterials in plants is more challenging than in mammalian cells or tissues due to the presence of plant cell wall, differences in membrane chemical compositions and significantly lower endocytic rate in plants.[5,13] Existing nanoparticle-based methods still rely heavily on tools like the gene gun, where DNA-coated gold microparticles are used as bullets for bombardment of plant cells and tissues to achieve gene transfer.[14] These methods require specialized, expensive equipment and lead to significant plant cell damage due to high delivery pressures.[15,16] To address these limitations, there is an urgent need to understand how nanoparticles interact with various biological membranes within plant cells. Such fundamental understanding will enable the rational design of nanoparticle formulations for targeted delivery and increased internalization efficiency without the aid of mechanical force or chemical treatments.

There have been significant successes in the use of mesoporous silica[5,7,17] or other nanomaterials such as carbon nanotubes[13,18] to deliver nucleic acids into plant cells. Besides nucleic acids, nanoparticles can also be functionalized with molecules such as fluorescent dyes for intracellular labelling in plants,[18] active molecules for tracking and sensing purposes,[19] and agrochemicals for crop health.[20] Targeted delivery of nanoparticles to certain regions of plant tissue

is also important for the creation of biomimetic systems such as light-harvesting apparatuses, photonic devices, emission sources for near-infrared communication to electronic devices, and carbon-negative temperature and environmental sensors.[19,21,22] We have previously shown that highly charged nanoceria, a nanoparticle-based reactive oxygen species (ROS) scavenger, and certain polymer-wrapped single-wrapped carbon nanotubes (SWNTs) localized within the chloroplasts when introduced to plant mesophyll tissue, enabling photosynthetic rate augmentation and extending the photoactive lifetime of extracted chloroplasts.[23,24] In recent work, we have demonstrated that the physical properties of nanoparticles can be tuned to control their localization in leaf mesophyll tissue to enable non-native functionalities such as light emission.[21] The ability to understand and control the transport of nanoparticles within living plant cells is therefore of practical and significant importance for various plant bioengineering applications, extending beyond plant genome engineering.[25] Nanomaterials have been shown to be able to traverse past the cellulosic cell wall due to their sizes[7,26,27] which allow them to passively enter through cell wall pores ranging from 5-20 nm in diameter.[28,29] However, to date, the mechanism of transport of nanoparticles past the plasma membrane and into the subcellular organelles remains unclear. Recent findings have suggested that the interaction between nanoparticles and lipid bilayers might contribute to the perceived ability of nanoparticles to passively transport past biological membranes.[30–34] In particular, asymmetric membrane composition and curvature were revealed by dissipative particle dynamics (DPD) simulations to strongly influence lipid – nanoparticle interaction and enhance penetration efficiency to above 90% under desirable conditions.[35] Atomistic simulation also presented the possibility of a rearrangement of zwitterionic lipid molecules in the contact area due to cation-lipid binding, resulting in a transient pore formation on the membrane.[34] Several mechanisms for nanoparticle transport past lipid bilayers have been proposed, such as passive penetration[18,36,37] and endocytosis,[13,38] but these mechanisms remain inconclusive and there remains a lack of a general, predictive model that can guide the rational design of nanoparticles for targeted delivery into plant tissues.

In this work, we present nanoparticle design principles based on experimental observations and mathematical modelling that determine the selective entry and subsequent subcellular distribution of nanomaterials into whole plant protoplasts. Our work represents one of first investigations into the mechanism of passive nanoparticle transport into plant cells, which is distinct from mechanisms proposed for nanoparticle uptake into mammalian cells.[39] Using imaging flow cytometry and fluorescence-activated cell sorting, we investigated the influence of cell morphology and cell type on nanoparticle uptake efficiency on a large number of cells (n > 8000). We further conducted a systematic investigation to explain the differences in nanoparticle internalization efficiency into whole cells (protoplasts) as opposed to organelles (chloroplasts) for plant systems. Our mathematical model, which we call Lipid Exchange Envelope Penetration (LEEP), can enable the rational design and targeted delivery of nano and biomaterials into specific compartments within plant cells without the use of physical, chemical or mechanical aid.

Results and Discussions

Charge and Size-Dependent Localization of Nanoparticles to Leaf Protoplasts

We investigated the mechanism of nanoparticle uptake with protoplasts – whole intact plant cells without cellulosic cell walls – as they are surrounded only by the plasma membrane which enables direct investigation of the interaction between nanoparticles and plant lipid bilayers. In addition, they are abundant and can be regenerated into whole plants, and therefore represent a versatile and convenient experimental system for plant biology studies.[40] Protoplasts were first prepared using a protocol as reported by Yoo et al.[41] from *Arabidopsis thaliana* plants grown in the laboratory. For all experiments, *Arabidopsis thaliana* protoplasts were incubated with nanoparticles for 16 hours at 4°C in the dark before immediate characterization, to exclude the possibility of active transport processes.[42] The nanoparticles used in this study are streptavidin-conjugated quantum dots

(SA-QD), Alexa Fluor 405-conjugated gold-cysteine nanoparticles (Au-Cys-AF405), Alexa Fluor 488-conjugated silica nanoparticles (SNP-AF488), dextran-coated nanoceria conjugated with Alexa Fluor 488 (dNC-AF488), and single-walled carbon nanotubes wrapped in various polymers such as chitosan (chi-SWNT), polyhistidine (pHis-SWNT) and 30-base sequence of ssDNA $(AT)_{15}$ (hereafter referred to as ss$(AT)_{15}$-SWNT). Confocal visible and Raman microscopy, near-infrared (NIR) microscopy and flow cytometry techniques were then used to study the distribution of nanoparticles within leaf protoplasts. Only healthy protoplasts, characterized by their spherical shape and fluorescein diacetate (FDA) staining,[43] were considered.

We observe that highly charged nanoparticles, such as Au-Cys-AF405 (-33 mV) and SWNTs coated with ss$(AT)_{15}$ (-48 mV), chitosan (+52 mV) and polyhistidine (+57 mV), are able to passively traverse the protoplast membrane and localize mostly in the chloroplasts within the protoplasts **(Figure 1a)**. This trend was observed for both positively and negatively charged nanoparticles, despite the fact that both protoplast and chloroplast membranes are negatively charged.[44]s The localization of SWNTs within the chloroplasts was confirmed using NIR microscopy (Figure 1b; Supplementary Figure S1) and Raman spectroscopy (Figure 2; Supplementary Figure S2). With Raman spectroscopy, confocal spatial mapping was performed to monitor the G-band intensity of SWNTs inside protoplasts (Figure 2a). G-band is an important optical feature of SWNT that is caused by planar vibrations of carbon atoms in tangential mode.[45] Heat map of this G-band intensity was then used to extract the three-dimensional spatial information of where SWNTs are located within protoplasts. The high G-peak intensity of SWNTs coincides with the location of chloroplasts within the protoplasts, confirming that SWNTs are mainly trapped inside the chloroplasts (Figure 2b and 2c). The high G-peak intensity outside the protoplasts indicate free SWNTs in solution that were not able to enter the protoplasts. Internalization of Au-Cys-AF405 within the chloroplasts inside protoplasts was separately confirmed via confocal microscopy (Supplementary Figure S3).

Interestingly, SA-QD (-23 mV), which had been previously found unable to penetrate the chloroplast membrane,[46] are observed to traverse past the protoplast membrane and localize within

the cytosol (Figure 3a). Propidium-iodide staining shows that SA-QD internalized protoplasts are still viable after nanoparticle internalization (Supplementary Figure S4). More neutrally-charged nanoparticles, such as dNC-AF488 (-1.8 mV), which have been found to effectively scavenge reactive oxygen species in isolated chloroplasts,[24] and SNP-AF488 (-2.4 mV), were not found within the protoplast interior (Figure 3c; Supplementary Figure S5). The size and zeta potential of nanoparticles investigated in this study are plotted in Figure 3b.

Mathematical Model Formulation and Model Significance

We had previously presented an experimentally validated Lipid Exchange Envelope Penetration (LEEP) model to describe the mechanism of nanoparticle transport into isolated chloroplasts.[46] In the LEEP model, the charged nanoparticles are assumed to induce image charge formation in the lipid bilayers, resulting in transmembrane potential drop across the lipid bilayers. This creates a driving force for charge-mediated and specific enthalpic interaction between the lipid bilayers and charged nanoparticle, which leads to softening of the lipid bilayers. The softened lipid membrane then allows for nanoparticle entry, during which lipid molecules will bind onto the nanoparticles through chemical interactions. The lipid-wrapped nanoparticles become kinetically trapped in the interior as the membrane reheals. The LEEP mechanisms are summarized by the mathematical model given in equation 1

$$\xi^{*} = \pm\left(\frac{\varepsilon_M + \varepsilon_W}{\varepsilon_W}\right)\left(\frac{d}{a}\right)e^{\kappa(d-a)}\sqrt{\frac{(\Gamma - a\gamma_0 + 4a\Delta\Delta H\rho_n)L}{2a\varepsilon_0\varepsilon_M\left(1-\frac{\varepsilon_M}{\varepsilon_W}\right)}} \qquad \text{(Equation 1)}$$

where ξ^{*} is the threshold zeta potential for nanoparticle entry, ε_M and ε_W are relative permittivity of the plant membrane and the medium respectively, d is the effective charge radius, a is the nanoparticle radius, κ^{-1} is the Debye-Huckel screening length, Γ is the pore line tension, γ_0 is the resting membrane tension, $\Delta\Delta H$ is the change in free energy due to lipid binding on nanoparticle, ρ_n is the lipid density on nanoparticle, and L is the approximate thickness of the membrane dielectric.

The protoplast system studied in this work is of substantially different length scales from the chloroplasts, with the chloroplasts contained within the protoplast envelope and being much smaller than the protoplast (typically 20-70 μm for the protoplast used in this study vs 3-10 μm for the chloroplast). In living plant cells, in contrast to isolated chloroplasts, nanoparticles have to traverse past both the protoplast plasma membrane and the chloroplast double lipid bilayers to localize within the chloroplast stroma, and it was unclear if the LEEP mechanism could describe the distribution of nanoparticles within the protoplasts. It was also unknown if the LEEP model, originally formulated based on chloroplast double lipid bilayers' properties, could describe the ability of nanoparticles to passively transport past the protoplast membrane, given that there are significant structural and biological differences between the protoplast and chloroplast membranes. Chloroplast is enveloped by outer and inner membranes largely composed of glycerolipids; the former is permeable to a large number of small molecules owing to the presence of porins, while the latter is selectively permeable to specific transport proteins crucial for photosynthesis.[47] On the other hand, protoplast only has one membrane which consists mostly of phospholipids.[48] In addition, the dielectric constant of protoplast membrane is different from that of the chloroplast membrane.[49] As a result, the nanoparticle-induced potential drops across the two membranes will be different. The average relative permittivity of protoplast membrane (ε_M = 7.8) is estimated to be higher than that of chloroplast membrane (ε_M = 2.2).[50] Physically, this means that the energy barrier for nanoparticle transport across protoplast membrane is lower, as reflected in the lower critical zeta potential value for nanoparticle penetration into protoplast interior compared to that required to traverse chloroplast double lipid bilayers (Figure 4). Furthermore, without the protection of plant cell wall, the protoplast membrane is known to be delicate and easily ruptured due to external handling such as electroporation and bombardment of nanoparticles.[51] This was not accounted for by the existing LEEP model, which only predicts the minimum surface charge that a nanoparticle of certain size has to possess in order to traffic past the membrane.

Consequently, an improved LEEP model was developed to predict the maximum nanoparticle surface charge that would allow the nanoparticle to interact with protoplast membrane without causing cell lysis. This was formulated by accounting for the maximum membrane and line tensions of the protoplast membrane. According to our LEEP mechanism, charged nanoparticles will induce a transmembrane potential drop across the lipid bilayer, which will then lead to pore formation. It follows that there should be a threshold transmembrane potential drop above which the pore radius will exceed the critical radius required to maintain membrane integrity.[52] We had previously modeled the lipid bilayer as a simple parallel plate capacitor in which the transmembrane potential drop affects the protoplast membrane tension as shown in equation 2

$$\gamma = \gamma_0 + \frac{\varepsilon_0 \varepsilon_M \left(1 - \frac{\varepsilon_M}{\varepsilon_W}\right)}{2L} V^2 \quad (2)$$

where V is the induced transmembrane potential drop. The induced electric potential is related to the nanoparticle surface potential, ξ, by equation 3 after accounting for the fictitious image charge formation inside the lipid membrane

$$V = \left(\frac{2\varepsilon_W}{\varepsilon_M + \varepsilon_W}\right)\left(\frac{\xi a e^{-\mathrm{K}(d-a)}}{d}\right) \quad (3)$$

Substituting equation 3 for V in equation 2 yields the following expression for nanoparticle surface charge

$$\xi = \pm\left(\frac{\varepsilon_M + \varepsilon_W}{\varepsilon_W}\right)\left(\frac{d}{a}\right) e^{\kappa(d-a)} \sqrt{\frac{(\gamma - \gamma_0)L}{2\varepsilon_0 \varepsilon_M \left(1 - \frac{\varepsilon_M}{\varepsilon_W}\right)}} \quad (4)$$

It is known that the maximum tension that the plant protoplast membrane can withstand prior to lysis is around 5 mN/m.[53,54] Solving equation 4 at the asymptotic limit $d = a$ with this threshold γ value

gives $\xi = \pm 78$ mV, which is the predicted maximum surface potential that any nanoparticle can have in order to penetrate the protoplast membrane without lysing the membrane.

Nanoparticle-induced pore formation also results in an increase in the free energy of the lipid membrane due to line tension at the edge of the pore. The maximum line tension for the pore to spontaneously reheal is estimated to be 30 pN.[55,56] Line tension higher than this threshold value would result in disruption of membrane curvature and ultimately cell lysis. Using this threshold value to solve equation 1 gives a relationship between the critical size and surface charge of nanoparticles above which protoplast lysing due to line tension is predicted to occur (Figure 4). A summary of known estimates of the model parameters used in this study is given in Table 1.

We note that our LEEP model gives estimated rather than strict predictions to determine the distribution of nanoparticles within plant cells. The model is consistent with experimental observations and can be used to explain why certain types of nanoparticles are able to traverse past the plant plasma membrane, for all nanoparticles investigated in this study and those reported in previous findings (Figure 4).[7,19,23,57] It predicts that both positive and negatively charged nanoparticles can enter the protoplasts and chloroplasts if the absolute value of their surface potential exceeds the size-dependent threshold value defined by the model lines (Figure 4). Our LEEP model also enables the rational design of nanoparticles to target different compartments within the plant cells. By tuning the zeta potential and dimension of nanoparticles, they can be designed to specifically target the protoplast cytosol, e.g. for nuclear transformation,[58] or the chloroplasts, e.g. for plastid engineering study[59] and photosynthetic activity augmentation.[23] The LEEP model also predicts that for very small nanoparticles ($a < 0.5$ nm), unphysical surface potentials are required to traverse past the protoplast membrane. The inability of DNA molecules (size of nucelotide ~ 0.34 nm) and small proteins to get into the protoplast interior without chemical or physical disturbances such as PEG-mediated transformation[60–62] and electroporation,[63–65] both of which destabilize the protoplast membrane, [66] is therefore consistent with our LEEP model predictions.

Influence of Protoplast Morphology and Cell Type on Nanoparticle Uptake

The proposed LEEP model successfully predicts the ability of nanoparticles to traverse the plant membrane barriers based on mechanistic steps formulated upon principles of lipid affinity, generalized membrane-nanoparticle electrostatic surface interaction and membrane mechanical properties. However, we would like to highlight that there are some limitations with the proposed model. Although the model can predict the fate of nanoparticles in protoplasts, it does not predict the efficiency of internalization. A systematic study was therefore conducted to investigate the optimum ratio of protoplast and nanoparticle concentration for efficient internalization. The uptake efficiency of ss$(AT)_{15}$-SWNT was found to increase with nanoparticle concentration until what we determined to be the optimum SWNT concentration of 12 mg/L (Figure 5a). Above this concentration, the viability of protoplasts, assessed by FDA staining, is significantly reduced (Figure 5a; Supplementary Figure S6). We postulate that at higher concentration of ss$(AT)_{15}$-SWNT, there is a higher frequency of contact between the lipid bilayers of protoplasts and nanoparticles, which contribute to the observed higher internalization efficiency. However, above the threshold concentration, the more frequent interactions between the lipid bilayers and the nanoparticle may induce pore formation in the plasma membrane at a time scale shorter than that required for the membrane to reheal. This leads to the formation of pores bigger than the critical pore size required to maintain protoplast integrity and ultimately membrane rupture.[67] Specifically, according to collision theory, the probability, p, of n nanoparticles ($n > 1$) interacting with the same region of the membrane in quick succession is related to the nanoparticle concentration, C, as $p \sim C^n$. Hence, the probability of membrane rupture will increase non-linearly with nanoparticle concentration and rupture will become more frequent with increasing concentration in a non-linear way.

Interestingly, even at the optimum concentration of nanoparticles, not all protoplasts show internalization of nanoparticles. It is commonly assumed that protoplasts are dedifferentiated cells and

therefore the tissues from which they are isolated are of little importance.[68] However, previous studies have shown that protoplasts isolated from different tissues exhibit significant differences in terms of promoter activity and vesicle trafficking.[68] We postulate that the morphological properties and identities of individual protoplast tissue type have an influence on their nanoparticle uptake. Herein, we demonstrate, for the first time, the application of imaging flow cytometry to characterize the heterogeneity of protoplasts and nanoparticle distribution within plant cells. Imaging flow cytometry platform allows for high-throughput visualization of fluorescence and morphometric characterization in single cells, enabling non-biased qualitative and quantitative analysis of subcellular distribution of nanoparticles.[69,70] This platform was used to perform qualitative and quantitative analysis of the SA-QD uptake efficiency of protoplasts with different sizes. The localization of SA-QD in the cytosol of the protoplasts confirmed earlier results which were obtained using confocal fluorescence microscopy (Figure 5b). The availability of a large data set of individual protoplasts (n ~ 8,000) also allowed reliable, rapid and convenient analysis on the influence of protoplast size on SA-QD uptake. We found that larger diameter protoplasts (diameter > 30 μm) show approximately 20% higher nanoparticle uptake efficiency than smaller protoplasts (diameter < 30 μm) (Figure 5c). The logarithmic plot of normalized SA-QD fluorescence intensity with protoplasts diameter shows a slope of 2.10 ± 0.08 (Figure 5d). This suggests that nanoparticle uptake efficiency is proportional to the surface area of protoplasts, which is consistent with our LEEP model. Larger protoplasts necessarily have a higher radius of curvature and thus experience higher membrane tension than smaller protoplasts for a given transmembrane pressure.[71] This lowers the barrier for penetration according to LEEP model (Supplementary Figure S7) and thus allows for easier entry of nanoparticles into larger diameter protoplasts than smaller protoplasts. In addition, there may also be increased frequency of collisions and interaction between nanoparticles and the lipid bilayers, which subsequently contributes to higher nanoparticle uptake rates in larger diameter protoplasts. Specifically, the capture probability of nanoparticles in a solution should scale linearly in nanoparticle

concentration but with the square of the protoplast radius. In the dilute Langmuir region, the number of internalized nanoparticles, N_i, can be estimated by equation 5:

$$N_i = P_{capture} 4\pi R^2 C_{np} \quad \text{(Equation 5)}$$

where $P_{capture}$ is the capture probability of nanoparticles, R is the protoplast radius and C_{np} is the concentration of nanoparticles in solution. The slope of 2.10 ± 0.08 obtained in log-log plot in Figure 5d thus supports the hypothesis that protoplast surface area is the primary determinant of nanoparticle internalization efficiency into protoplasts.

Fluorescence-activated cell sorting (FACS) was also used to sort protoplasts into sub-populations with different chloroplast content based on chlorophyll autofluorescence (Figure 5e and 5f). Protoplasts with higher chloroplast content, *e.g.* mesophyll and guard cell protoplasts, were found to exhibit higher internalization efficiency of SWNTs than those with low chloroplast content, *e.g.* epidermal cells (Figure 5g). These findings are consistent with our hypothesis that different characteristics and cell types of protoplasts affect nanoparticle internalization. Besides protoplast size and chlorophyll content, we note that there are other physical and chemical attributes of protoplasts that may result in heterogeneity of nanoparticle uptake distribution. For instance, previous studies have found that there is a wide distribution of dielectric constant of protoplast membrane, which affects the magnitude of nanoparticle-induced transmembrane potential.[72] However, to the best of our knowledge, this work represents the first experimental study on confirming the influence of different characteristics of protoplasts on nanoparticle uptake.

Effect of Membrane Chemical Compositions on Nanoparticle-Lipid Interaction

From our experimental results, we note that we observed a lower internalization efficiency of ss$(AT)_{15}$-SWNT into protoplasts (~40% from Figure 5a) compared to isolated chloroplasts as reported in our previous work (70-80%).[23] We propose that the lipid composition of protoplast and chloroplast membrane influences the lipid-nanoparticle interaction which subsequently affects the penetration

efficiency of the nanoparticles. Previous studies have found that lipid headgroups and tail lengths have significant influence on lipid-nanoparticle interaction.[73–75] Plant protoplast membrane typically consists of a high proportion of phospholipids, specifically unsaturated phosphocholines (PC),[76] while chloroplast possesses two membranes rich in glycerolipids.[49,77]

To investigate the specific interaction between different types of lipids and nanoparticles, two distinct multilamellar liposome systems were synthesized from 16:0-18:2 PC and a mixture of digalactosyldiacylglycerol (DGDG) and monogalactosyldiacylglycerol (MGDG) to represent the protoplast and chloroplast membranes respectively. Laurdan (6-lauroyl-2-dimethylaminonaphthalene), a fluorescent probe that partitions into the lipid phase with negligible solubility in aqueous phase,[78,79] was used to assess the degree of interaction between nanoparticle and the membrane systems. Upon exposure of ss$(AT)_{15}$-SWNT, both laurdan-embedded glycerolipid and phospholipid liposomes display a decrease in fluorescence intensity (Figure 6a), which indicates a less ordered membrane structure in the headgroup region.[80] This observation is consistent with our LEEP model, which assumes that there are chemical and electrostatic interactions between nanoparticles and lipid bilayers that lead to membrane softening. The adsorption of lipid molecules on SWNT surface does not induce any significant change in membrane fluidity as measured by shifts in laurdan fluorescence (Supplementary Figure S8). The laurdan intensity quenching is found to be more significant for glycerolipid than phospholipid liposomes, suggesting that ss$(AT)_{15}$-SWNT interact more strongly with glycerolipid liposomes than with phospholipid liposomes. This is further confirmed by the trend in intensity attenuation and solvatochromic shift of ss$(AT)_{15}$-SWNT near-infrared emission spectra (Figure 6b). Incubation of ss$(AT)_{15}$-SWNT with glycerolipids results in higher quenching of fluorescence intensity and more pronounced blue-shift in emission wavelength maxima relative to that with phospholipids. This was observed for almost all chiralities of HiPCo nanotubes (Figure 6c). Recently, Jena et al.[81] confirmed through molecular dynamics simulation and *in vivo* experiments that the binding of lipids onto DNA-wrapped carbon nanotube surface decreases the water density around the nanotubes, resulting in a decrease in the nanotube emission wavelength.

The shift in SWNT fluorescence emission peaks can be explained by the change in local dielectric environment of the SWNT surface,[82] which subsequently affects the polarizability of the excitons along the nanotube surface.[83] Random orientation of the dipole moments in proximity of the SWNT surface can induce the rearrangement of solvent molecules to solvate the dipole, resulting in fluctuating electric fields. The electric fields can then cause a shift in electronic transition energies of SWNT (solvent Stark effect), which can be described by the empirical form in equation 6[82]

$$(E_{ii})^2 \Delta E_{ii} = -Lk\left[\frac{2(\varepsilon-1)}{2\varepsilon+1} - \frac{2(\eta^2-1)}{2\eta^2+1}\right]\left(\frac{1}{R^4}\right) = \frac{C}{R^4} \quad \text{(Equation 6)}$$

where E_{ii} is the optical transition energy, ΔE_{ii} is the difference between the optical transition energy in the dielectric environment and that of pristine SWNT suspended in air, L is a fluctuation factor, k is a proportionality constant, ε is the solvent dielectric constant, η is the refractive index and R is the nanotube radius. All of the parameters specific to a SWNT chirality are represented by the constant C.

The solvatochromic shifts, $(E_{ii})^2 \Delta E_{ii}$, were calculated from individual emission peaks of different chiralities in the HiPCo SWNT samples, as described previously.[84] They were then plotted as a function of SWNT diameter to the power of negative 4 (d^{-4}) for all chiralities and a linear regression was performed (Figure 6d). The slopes of the best-fit lines were compared with the slope of a reference system, SWNT suspended in N-methyl-2-pyroolidone (NMP),[85] and were then used to approximate the effective local dielectric constant, ε_{eff}, near the SWNT surface:

$$\frac{C}{C_{NMP}} = \frac{\frac{\varepsilon_{eff}-1}{2\varepsilon_{eff}+1} - \frac{\eta^2-1}{2\eta^2+1}}{\frac{\varepsilon_{NMP}-1}{2\varepsilon_{NMP}+1} - \frac{\eta_{NMP}^2-1}{2\eta_{NMP}^2+1}} \quad \text{(Equation 7)}$$

where C_{NMP} = 0.060 eV^{3}nm^4, ε_{NMP} = 32.2 and η_{NMP} = 1.47. The refractive index of DNA-wrapped SWNT was assumed to be equal to that of water (η = 1.333) and unchanged upon the addition of phospholipids or glycerolipids. The relative surface coverage of SWNT with respect to the DNA wrapping and lipid molecules can then be estimated from the effective dielectric constant assuming a linear contribution from the solvent molecules and the polymer wrapping

$$\varepsilon_{eff} = \chi\varepsilon_p + (1-\chi)\varepsilon_w \quad \text{(Equation 8)}$$

where χ is the relative surface coverage, ε_p is the dielectric constant of the wrapping polymer (ε_p = 4 for DNA wrapping[86]) and ε_W is the dielectric constant of the solvent (ε_W = 80 for water). Based on the relative values of χ, the addition of phospholipids and glycerolipids to ss(AT)$_{15}$-SWNT resulted in a higher nanotube surface coverage compared to SWNT wrapped in ss(AT)$_{15}$, confirming the binding of lipid molecules onto the nanotube surface (Figure 6e; Supplementary Table S1). However, the more pronounced blue shift after the addition of glycerolipids, observed in Figure 6c, translates to a higher relative surface coverage as compared to the addition of phospholipids. This indicates that ss(AT)$_{15}$-SWNT could interact to a higher extent with glycerolipids than phospholipids, resulting in a lower surface exposure of nanotubes to water molecules and thus a decrease in the local dielectric environment. The stronger binding of glycerolipids onto the nanotube surface leads to a larger solvatochromic response in emission wavelengths of ss(AT)$_{15}$-SWNT. This explains why charged nanoparticles can still enter the chloroplasts after traversing past the protoplast membrane. We postulate that the weaker interaction between protoplasts and charged nanoparticles lead to incomplete lipid binding onto the surface of nanoparticles. The free sites on the nanoparticles can then further interact with the double lipid bilayers of the chloroplasts, allowing entry of nanoparticles into the chloroplasts.

CONCLUSIONS

Despite recent advances in the use of nanomaterials as molecular transporters across biological systems, the incorporation of nanomaterials into specific compartments within plant cells remains challenging due to unclear mechanisms surrounding nanoparticle interaction with biological membranes in plants. In this work, we have conducted a mechanistic study to elucidate the transport and subcellular distribution of various nanoparticles within plant protoplasts. The distribution of nanoparticles within the protoplasts is found to be controlled mainly by the size and the magnitude, but not the sign, of the zeta potential of nanoparticles. Based on these experimental findings, we have proposed a LEEP mathematical model which can guide the rational design of nanoparticles for targeted delivery into plant cells and subcellular organelles. In addition, using high-throughput imaging flow cytometry and FACS, we found that morphological characteristics and cell type of protoplasts influence nanoparticle internalization efficiency. Nanoparticle interaction with different biological membranes within plant cells was also investigated. Our study discerned significant differences in nanoparticle-lipid interaction strength between glycerolipids and phospholipids, which are the preponderant lipid constituents in chloroplast and plasma membrane respectively. As the first mechanistic study to yield rational design principles to control nanoparticle subcellular distribution in plant cells, we expect our model to have broad utility in plant engineering applications and contribute to furthering our fundamental understanding of plant biology.

EXPERIMENTAL SECTION

Preparation of ssDNA and polymer wrapped SWNTs. HiPCo SWNTs (Lot # HS27-104) were purchased from NanoIntegris. Single stranded DNA polymers with sequence $(AT)_{15}$ ($ss(AT)_{15}$) were purchased from Integrated DNA Technologies, Inc. 1 mg of $ss(AT)_{15}$ was added to 0.25 mg of HiPCo SWNTs in 1 mL of 70 mM of sodium chloride solution. The mixture was then sonicated with 3 mm probe tip (Cole Parmer) for 20 minutes at 40% amplitude. The sample was subsequently centrifuged twice at 16,000 g for 90 minutes to remove unsuspended SWNT aggregates. The concentration of suspended SWNTs was determined by measuring the SWNT absorbance at 632 nm. For preparation of chitosan-wrapped SWNTs, HiPCo SWNTs were sonicated in 0.25 wt. % chitosan and 0.3 wt. % acetic acid for 40 minutes at 40% amplitude with 3 mm tip sonicator. For preparation of poly-L-histidine SWNTs, 0.75 mg poly-L-histidine was added to 0.25 mg of HiPCo SWNTs in 1 mL of de-ionized water containing 0.3 wt. % acetic acid. The mixture was sonicated with 3 mm probe tip for 20 minutes at 40% amplitude.

Preparation of Gold-Cys-AF405 Nanoparticles. Gold nanoparticles (10 nm, 0.05 mg/mL) were purchased from Nanocomposix®. Labelling of gold nanoparticles with fluorescent dye was achieved as previously described.[46] Briefly, L-cysteine (Sigma-Aldrich) was reacted with 1 equiv. of Alexa Fluor 405-NHS (Invitrogen) in 400 µL of PBS for 1 h at room temperature. 2 mL of gold nanoparticle solution (0.025 mg/mL) was mixed with cysteine-Alexa Fluor 405 conjugate for 2-3 h at room temperature. The resulting solution was purified by centrifugation at 2000 g several times with DI water using 50,000 centrifugal filter unit (Millipore Inc.) to wash off unreacted cysteine-Alexa Fluor 405 conjugate.

Preparation of dextran-wrapped nanoceria (dNC). The dNC were prepared as previously described with modifications.[24,87] Briefly, 2 mg of Alexa Fluor 488-labelled dextran (Invitrogen, MW = 10,000) was dissolved in 20 mL of DI water. Approximately 0.55 mg of cerium nitrate

hexahydrate (Sigma-Aldrich) was dissolved in the dextran solution, which was then adjusted to pH 7.5 with ammonium hydroxide (Sigma Aldrich, 27% w/w). The solution was subsequently stirred for 3 hours to allow for complete dextran complexation. The resulting mixture was then centrifuged at 2500 g several times with 10,000 MWCO centrifugal filter unit (Milipore) to wash off free, unreacted dye.

Preparation of AF488-labelled silica nanoparticles (SNP-AF488). SNP-AF488 was prepared as previously described.[21] Briefly, (3-glycidyloxypropyl)trimethoxysilane (GPTS) was added to a mixture of 75% ethanol/water and incubated at room temperature for 1 h for complete hydrolysis. 125 µL of the mixture was then added to 0.5 mL of 10 nm silica nanoparticles (10 mg/ml, Nanocomposix, CA, USA) in 2.5 mL of 80% of ethanol/water. The resulting mixture was incubated for 24 h and washed thoroughly with ethanol and water using 30,000 MWCO centrifugal filter unit (Milipore). 200 µg of Alexa Fluor 488-cadaverine (Invitrogen) was added to 2 mL of 1 mg/mL nanoparticle suspension. After 24 h incubation at 65˚C, Alexa Fluor 488 conjugated silica nanoparticles (SNP-AF488) were washed with water thoroughly until the filtrate had no detectable absorbance at 493 nm.

Nanoparticle size and zeta potential measurement. The size distribution of nanoparticles was determined by single particle tracking analysis with NanoSight LM10 (Malvern Instruments Ltd). Dynamic Light Scattering (DLS) and Phase Analysis Light Scattering (PALS) zeta potential instrument were used to measure the nanoparticle surface potential and confirm the nanoparticle size distribution (NanoBrook ZetaPALS Potential Analyzer).

Plant growth. Seeds of *Arabidopsis thaliana* ecotype Columbia (Col-0) were obtained from Arabidopsis Biological Resource Center (ABRC). The seeds were stratified for 48 h at 4^{o}C and soil-grown for 3-4 weeks in a plant growth chamber (Adaptis 1000, Conviron, Canada) at a set condition of 10-hour photoperiod at 200 µmol s^{-1} m^{-2}, 60% relative humidity, day and night temperatures of 22^{o}C and 18^{o}C respectively.

Protoplast isolation. Protoplasts were isolated from Arabidopsis thaliana leaves as described by Yoo et al.[41] with modifications. Several healthy, well-expanded leaves from plantlets (20 d of age) were picked and cut into 1-2 mm strips with a razor blade. The leaf strips were immediately transferred into 20 mL enzyme solution (1.5% cellulase R-10, 0.5% maceroezyme R-10, 20 mM MES (pH 5.7), 0.4 M mannitol, 20 mM KCl, and 10 mM $CaCl_2$). The solution was vacuum infiltrated for 30 minutes and incubated in the dark for 3 hours without stirring to allow for enzyme digestion. Undigested leaf tissue was filtered using 75 μm nylon mesh and the filtrates were centrifuged at 200 g for 3 min to pellet the protoplasts in a round-bottomed tube. The pellet was then re-suspended in MMG solution (0.4 M mannitol, 4 mM MES (pH 5.7), and 15 mM $MgCl_2$) by gentle swirling. The centrifugation and re-suspension process was repeated three times to achieve high purity of viable protoplasts. The viability of protoplasts was determined by staining the protoplasts with fluorescein diacetate (FDA), as described elsewhere.[51] The total protoplasts yield was determined by a hemocytometer. Only freshly isolated protoplasts were used for nanoparticle uptake experiments.

Fluorescent confocal micrographs. 100 μL of protoplast solution (approximately 10^5 cells/mL) were incubated with Au-Cys-AF405 (50 μg/mL), SNP-AF488 (0.1 mg/mL), dNC-AF488 (50 nM) and SA-QD (50 nM) for 24 hours. After the incubation, unless otherwise noted, the nanoparticle-protoplast suspension was washed by centrifugation at 200 g for 5 minutes to remove broken protoplasts and free nanoparticles in suspension. 90% of the supernatant was then removed and the protoplasts were gently re-suspended in MMG solution prior to imaging. For confocal imaging, a droplet of the protoplast suspension was placed on a 35 mm poly-d-lysine coated glass bottom dish (Mattek Corporation). Confocal images were taken in a Zeiss LSM 710 microscope with 40x water immersion objective. Au-Cys-AF405 nanoparticles were excited with a 405 nm laser and their emission recorded from 420 to 500 nm. SA-QD were excited with a 405 nm laser with emission channel from 525 to 575 nm. dNC-AF488 and SNP-AF488 were excited with 488 nm laser and their emission monitored from 510 to 580 nm. Chloroplast autofluorescence imaging was obtained by excitation near the absorbance

peak of chlorophyll with a 633 nm laser and emission channel between 660 and 750 nm. SA-QD internalized protoplasts were also stained with propidium iodide (20 µg/mL) to check their viability after nanoparticle internalization. Propidium iodide was excited with 514 nm with emission channel from 590 to 650 nm.

NIR fluorescent microscopy. A Zeiss Axiovision inverted microscope attached to a 2D InGaAs OMA-V imaging array (Princeton Instruments) was used to visualize the localization of SWNTs in protoplasts. A droplet of the protoplast suspension was placed on a 35 mm poly-d-lysine coated glass bottom dish (Mattek Corporation) and viewed using 63x oil-immersion objective under brightfield. The sample was then illuminated with 785 nm photodiode laser (Invictus) and the NIR fluorescence of SWNTs was monitored with 1100 nm long pass emission filter (Chroma) to minimize chloroplast autofluorescence.

Confocal Raman spectroscopy. Raman maps were acquired in a confocal Raman spectrometer HR-800 (Horiba BY) using a 785 nm laser source. A droplet of protoplast suspension was introduced to a microscope slide and covered with a cover slip. The edges of the cover slip were carefully sealed to prevent evaporation. Samples were focused on a 50x objective (NA = 0.75) with pinhole of 50 µm and spectra were obtained with 10 s exposure time. 3D Raman map was plotted in Matlab R2015b.

Flow cytometry analysis for protoplasts separation into sub-populations. For protoplasts sorting, only freshly isolated protoplasts were used. Protoplasts were sorted according to their chlorophyll autofluorescence, as a proxy of chloroplast content, using FACSAria (BD Biosciences) equipped with 130 µm nozzle with a system pressure up to 30 psi. The sheath fluid composition was 0.4 M mannitol buffered with 4 mM MES at pH 5.7 to maintain protoplast osmolarity during sorting. Gating was defined on a dotplot of red (695/40 nm; y-axis) against green (530/30 nm; x-axis) fluorescence. The protoplasts were sorted into 5 mL collection tubes containing 1 mL of 0.4 M mannitol solution. Protoplast concentration for each sub-population was then adjusted to 10^5 cells/mL and the cells were

then incubated with 12 mg/mL ss$(AT)_{15}$-SWNTs. Three biological replicates were used to determine the nanoparticle uptake efficiency in each sub-population, with at least 80 protoplasts were analyzed in each replicate.

Imaging flow cytometry. 80 µL aliquots of protoplast-nanoparticle suspension were analyzed using five-laser two-camera ImageStream II imaging flow cytometer (Amnis, Seattle, WA). For each sample, approximately 80,000 protoplasts were collected at a rate of 1,000 to 2,000 cells per second. SA-QD and chlorophyll autofluorescence were excited using 405 nm and 488 nm laser, and emissions were captured in the range of 505-570 nm (Channel 8) and 660-740 nm (Channel 5) respectively. Brightfield image of individual protoplasts was also captured for morphological analysis of single cells. A 650 short pass filter and a compensation matrix, calculated from pure protoplast suspensions excited with identical laser settings, were employed to minimize the cross-talking between channels. Images were captured with INSPIRE acquisition software (Amnis v.6.1) utilizing 40x magnification. Post-acquisition data analysis was performed using IDEAS software (Amnis v.6.2.64) and Matlab R2015b. Cell viability was determined by defining gates on the aspect ratio of the protoplasts and only viable protoplasts were further analyzed. For analysis, 3 biological replicates were performed and for each biological replicate, at least 8,000 protoplasts were analyzed.

Liposome preparation. Liposomes were prepared as described previously with modifications.[80] Laurdan (15 µM) was mixed with the major constituent of protoplast phospholipids, 16:0-18:2 PC (1 mM), or the most common chloroplast glycerolipids, DGDG (0.7 mM) and MGDG (0.3 mM) (Avanti Lipids) in chloroform-methanol (1:1). The solvent was evaporated under oxygen-free nitrogen flow and further incubated in vacuum chamber for 1 h to remove any trace of solvent. The dry lipid films were pre-hydrated in 3 mL of sterile PBS buffer 1X and heated above the lipids gel-fluid transition temperature at 80°C. Liposomes were formed by vortexing for 5 x 30 s, reheating the sample between each vortexing cycle. The fluorescence of laurdan-labelled liposome with ss$(AT)_{15}$-SWNT was measured using a Varioskan flash plate reader 3001 (Thermo) in the range of 410 – 650 nm with 390

nm excitation. Laurdan generalized polarization (Gp) was calculated as described in Szilagyi et al.[80] To investigate the effect of lipid interaction on ss(AT)$_{15}$-SWNT NIR fluorescence, lipids were added to ss(AT)$_{15}$-SWNT at a final concentration of 0.2 wt. %, above their critical micelle concentrations (~ 0.1 wt. %).[75] The resultant mixture was vortexed to ensure mixing and centrifuged several times with water to remove excess lipid molecules before NIR fluorescence measurement is obtained.

AUTHOR INFORMATION

Corresponding Author

*E-mail: strano@mit.edu. Phone: 617.324.4323. Fax: 617.258.8824.

Author Contributions

The manuscript was written through contributions by T.T.S.L., M.H.W., S.K., V.B.K., and M.S.S. Experiments were designed and performed by T.T.S.L., M.H.W., S.K., and R.S. Protoplast isolation work was done by T.T.S.L. and R.S. All authors have revised the manuscript and given their approval of the final version.

Notes

The authors declare no competing financial interest.

Supporting Information

Supporting Information is available from the Wiley Online Library or from the author.

ACKNOWLEDGEMENTS

We acknowledge support of Disruptive & Sustainable Technology for Agricultural Precision (DiSTAP), Sime Darby Malaysia, Temasek Life Science Singapore and U.S. Department of Energy, Office of Science, Basic Energy Sciences under Award grant number DE-FG02-08ER46488 Mod 0008. T.T.S.L. and M.H.W. are supported on a graduate fellowship by the Agency of Science, Research and Technology Singapore. V.B.K. is supported by The Swiss National Science Foundation (project No. P2ELP3_162149). The authors wish to thank Scott Mordecai in the Department of Pathology Flow and Image Cytometry Core (Massachusetts General Hospital) for help with imaging flow cytometry, and Michael Waring at the Ragon Institute for help with FACS. The Amnis ImageStream was purchased using an NIH Shared Instrumentation Grant 1S10OD012027-01A1.

REFERENCES

[1] D. J. Bharali, I. Klejbor, E. K. Stachowiak, P. Dutta, I. Roy, N. Kaur, E. J. Bergey, P. N. Prasad, M. K. Stachowiak, *Proc. Natl. Acad. Sci. U. S. A.* **2005**, *102*, 11539.
[2] D. Luo, W. M. Saltzman, *Nat. Biotechnol.* **2000**, *18*, 893.
[3] D. Pantarotto, R. Singh, D. McCarthy, M. Erhardt, J. P. Briand, M. Prato, K. Kostarelos, A. Bianco, *Angew. Chemie-International Ed.* **2004**, *43*, 5242.
[4] S. T. Guo, Y. Y. Huang, Q. A. Jiang, Y. Sun, L. D. Deng, Z. C. Liang, Q. A. Du, J. F. Xing, Y. L. Zhao, P. C. Wang, A. J. Dong, X. J. Liang, *ACS Nano* **2010**, *4*, 5505.
[5] F. Torney, B. G. Trewyn, V. S. Y. Lin, K. Wang, *Nat. Nanotechnol.* **2007**, *2*, 295.
[6] A. T. Silva, N. Alien, C. M. Ye, J. Verchot, J. H. Moon, *BMC Plant Biol.* **2010**, *10*, 14.
[7] F. P. Chang, L. Y. Kuang, C. A. Huang, W. N. Jane, Y. Hung, Y. I. C. Hsing, C. Y. Mou, *J. Mater. Chem. B* **2013**, *1*, 5279.
[8] G. S. Demirer, M. P. Landry, *Chem. Eng. Prog.* **2017**, *113*, 40.
[9] S. Naqvi, A. N. Maitra, M. Z. Abdin, M. Akmal, I. Arora, M. Samim, *J. Mater. Chem.* **2012**, *22*, 3500.
[10] X. X. He, K. M. Wang, W. H. Tan, B. Liu, X. Lin, C. M. He, D. Li, S. S. Huang, J. Li, *J. Am. Chem. Soc.* **2003**, *125*, 7168.
[11] Y. Wu, J. A. Phillips, H. Liu, R. Yang, W. Tan, *ACS Nano* **2008**, *2*, 2023.
[12] S. Huo, S. Jin, X. Ma, X. Xue, K. Yang, A. Kumar, P. C. Wang, J. Zhang, Z. Hu, X.-J. Liang, *ACS Nano* **2014**, *8*, 5852.
[13] Q. Liu, B. Chen, Q. Wang, X. Shi, Z. Xiao, J. Lin, X. Fang, *Nano Lett.* **2009**, *9*, 1007.
[14] T. M. Klein, E. D. Wolf, R. Wu, J. C. Sanford, *Nature* **1987**, *327*, 70.
[15] J. A. Russell, M. K. Roy, J. C. Sanford, *Plant Physiol.* **1992**, *98*, 1050.
[16] A. M. Husaini, M. Z. Abdin, G. A. Parray, G. S. Sanghera, I. Murtaza, T. Alam, D. K. Srivastava, H. Farooqi, H. N. Khan, *GM Crops* **2010**, *1*, 276.
[17] B. Xia, C. Dong, W. Y. Zhang, Y. Lu, J. H. Chen, J. S. Shi, *Sci. China-Life Sci.* **2013**, *56*, 82.
[18] M. F. Serag, N. Kaji, E. Venturelli, Y. Okamoto, K. Terasaka, M. Tokeshi, H. Mizukami, K. Braeckmans, A. Bianco, Y. Baba, *ACS Nano* **2011**, *5*, 9264.
[19] M. H. Wong, J. P. Giraldo, S. Y. Kwak, V. B. Koman, R. Sinclair, T. T. S. Lew, G. Bisker, P. W. Liu, M. S. Strano, *Nat. Mater.* **2017**, *16*, 264.
[20] N. Kottegoda, C. Sandaruwan, G. Priyadarshana, A. Siriwardhana, U. A. Rathnayake, D. M. B. Arachchige, A. R. Kumarasinghe, D. Dahanayake, V. Karunaratne, G. A. J. Amaratunga, *ACS Nano* **2017**, *11*, 1214.
[21] S. Y. Kwak, J. P. Giraldo, M. H. Wong, V. B. Koman, T. T. S. Lew, J. Ell, M. C. Weidman, R. M. Sinclair, M. P. Landry, W. A. Tisdale, M. S. Strano, *Nano Lett.* **2017**, *17*, 7951.
[22] R. Di Giacomo, C. Daraio, B. Maresca, *Proc. Natl. Acad. Sci. U. S. A.* **2015**, *112*, 4541.
[23] J. P. Giraldo, M. P. Landry, S. M. Faltermeier, T. P. McNicholas, N. M. Iverson, A. A. Boghossian, N. F. Reuel, A. J. Hilmer, F. Sen, J. A. Brew, M. S. Strano, *Nat. Mater.* **2014**, *13*, 400.
[24] A. A. Boghossian, F. Sen, B. M. Gibbons, S. Sen, S. M. Faltermeier, J. P. Giraldo, C. T. Zhang, J. Q. Zhang, D. A. Heller, M. S. Strano, *Adv. Energy Mater.* **2013**, *3*, 881.
[25] S. Y. Kwak, M. H. Wong, T. T. S. Lew, G. Bisker, M. A. Lee, A. Kaplan, J. Y. Dong, A. T. Liu, V. B. Koman, R. Sinclair, C. Hamann, M. S. Strano, *Annu. Rev. Anal. Chem.* **2017**, *10*, 113.
[26] S. J. Lin, J. Reppert, Q. Hu, J. S. Hudson, M. L. Reid, T. A. Ratnikova, A. M. Rao, H. Luo, P.

C. Ke, *Small* **2009**, *5*, 1128.
[27] D. H. Lin, B. S. Xing, *Environ. Sci. & Technol.* **2008**, *42*, 5580.
[28] C. Rondeau-Mouro, D. Defer, E. Leboeuf, M. Lahaye, *Int. J. Biol. Macromol.* **2008**, *42*, 83.
[29] N. Carpita, D. Sabularse, D. Montezinos, D. P. Delmer, *Science (80-.).* **1979**, *205*, 1144.
[30] S. Pogodin, N. K. H. Slater, V. A. Baulin, *ACS Nano* **2011**, *5*, 1141.
[31] P. Gkeka, L. Sarkisov, P. Angelikopoulos, *J. Phys. Chem. Lett.* **2013**, *4*, 1907.
[32] Z. L. Li, H. M. Ding, Y. Q. Ma, *Soft Matter* **2013**, *9*, 1281.
[33] S. Pogodin, M. Werner, J. U. Sommer, V. A. Baulin, *ACS Nano* **2012**, *6*, 10555.
[34] E. Heikkila, H. Martinez-Seara, A. A. Gurtovenko, M. Javanainen, H. Hakkinen, I. Vattulainen, J. Akola, *J. Phys. Chem. C* **2014**, *118*, 11131.
[35] H. M. Ding, W. D. Tian, Y. Q. Ma, *ACS Nano* **2012**, *6*, 1230.
[36] A. Verma, O. Uzun, Y. H. Hu, Y. Hu, H. S. Han, N. Watson, S. L. Chen, D. J. Irvine, F. Stellacci, *Nat. Mater.* **2008**, *7*, 588.
[37] T. T. Wang, J. Bai, X. Jiang, G. U. Nienhaus, *ACS Nano* **2012**, *6*, 1251.
[38] E. Etxeberria, P. Gonzalez, E. Baroja-Fernandez, J. P. Romero, *Plant Signal. & Behav.* **2006**, *1*, 196.
[39] Q. Mu, G. Jiang, L. Chen, H. Zhou, D. Fourches, A. Tropsha, B. Yan, *Chem. Rev.* **2014**, *114*, 7740.
[40] J. Sheen, *Plant Physiol.* **2001**, *127*, 1466.
[41] S. D. Yoo, Y. H. Cho, J. Sheen, *Nat. Protoc.* **2007**, *2*, 1565.
[42] J. Rosenbluh, S. K. Singh, Y. Gafni, A. Graessmann, A. Loyter, *Biochim. Biophys. Acta-Biomembranes* **2004**, *1664*, 230.
[43] E. C. T. Yeung, C. Stasolla, M. J. Sumner, B. Q. Huang, *Plant Microtechniques and Protocols*, Springer, **2015**.
[44] T. Nagata, G. Melchers, *Planta* **1978**, *142*, 235.
[45] M. S. Dresselhaus, G. Dresselhaus, R. Saito, A. Jorio, in *Carbon Nanotub. Quantum Cylind. Graphene* (Eds: S. Saito, A. Zettl), **2008**, pp. 83–108.
[46] M. H. Wong, R. P. Misra, J. P. Giraldo, S. Y. Kwak, Y. Son, M. P. Landry, J. W. Swan, D. Blankschtein, M. S. Strano, *Nano Lett.* **2016**, *16*, 1161.
[47] M. A. Block, R. Douce, J. Joyard, N. Rolland, *Photosynth. Res.* **2007**, *92*, 225.
[48] M. R. Sussman ', J. F. Harper, *Plant Cell* **1989**, *1*, 953.
[49] P. J. Quinn, W. P. Williams, *Prog. Biophys. & Mol. Biol.* **1978**, *34*, 109.
[50] K. Asami, T. Yamaguchi, *Biophys. J.* **1992**, *63*, 1493.
[51] R. Lei, W. J. Qiao, F. Hu, H. S. Jiang, S. F. Zhu, *Methodsx* **2015**, *2*, 24.
[52] T. Tryfona, M. T. Bustard, *Biotechnol. Bioeng.* **2006**, *93*, 413.
[53] J. Wolfe, P. L. Steponkus, *Plant Physiol.* **1983**, *71*, 276.
[54] P. L. Steponkus, *Annu. Rev. Plant Physiol. Plant Mol. Biol.* **1984**, *35*, 543.
[55] A. Kell, R. W. Glaser, *J. Theor. Biol.* **1993**, *160*, 41.
[56] C. M. Rosetti, G. G. Montich, C. Pastorino, *J. Phys. Chem. B* **2017**, *121*, 1587.
[57] G. S. Demirer, R. Chang, H. Zhang, L. Chio, M. P. Landry, *bioRxiv* **2017**, 179549.
[58] S. Abel, A. Theologis, *Plant J.* **1994**, *5*, 421.
[59] Y. H. Lu, H. Rijzaani, D. Karcher, S. Ruf, R. Bock, *Proc. Natl. Acad. Sci. U. S. A.* **2013**, *110*, E623.
[60] F. A. Krens, L. Molendijk, G. J. Wullems, R. A. Schilperoort, *Nature* **1982**, *296*, 72.

[61] A. Hayashimoto, Z. J. Li, N. Murai, *Plant Physiol.* **1990**, *93*, 857.
[62] I. Negrutiu, R. Shillito, I. Potrykus, G. Biasini, F. Sala, *Plant Mol. Biol.* **1987**, *8*, 363.
[63] M. Nishiguchi, W. H. R. Langridge, A. A. Szalay, M. Zaitlin, *Plant Cell Rep.* **1986**, *5*, 57.
[64] M. Fromm, L. P. Taylor, V. Walbot, *Proc. Natl. Acad. Sci. U. S. A.* **1985**, *82*, 5824.
[65] H. Jones, G. Ooms, M. G. K. Jones, *Plant Mol. Biol.* **1989**, *13*, 503.
[66] B. Hahnhagerdal, K. Hosono, A. Zachrisson, C. H. Bornman, *Physiol. Plant.* **1986**, *67*, 359.
[67] T. Ohshima, M. Sato, *Recent Prog. Biochem. Biomed. Eng. Japan I* **2004**, *90*, 113.
[68] M. Faraco, G. Pietro Di Sansebastiano, K. Spelt, R. E. Koes, F. M. Quattrocchio, *Plant Physiol.* **2011**, *156*, 474.
[69] N. S. Barteneva, E. Fasler-Kan, I. A. Vorobjev, *J. Histochem. & Cytochem.* **2012**, *60*, 723.
[70] D. A. Basiji, W. E. Ortyn, L. Liang, V. Venkatachalam, P. Morrissey, *Clin. Lab. Med.* **2007**, *27*, 653.
[71] C. E. Morris, U. Homann, *J. Membr. Biol.* **2001**, *179*, 79.
[72] P. Wanichapichart, S. Bunthawin, A. Kaewpaiboon, K. Kanchanapoom, *ScienceAsia* **2002**, *28*, 113.
[73] H. Lee, H. Kim, *J. Phys. Chem. C* **2012**, *116*, 9327.
[74] H. Lee, *J. Phys. Chem. B* **2013**, *117*, 1337.
[75] Y. Wu, J. S. Hudson, Q. Lu, J. M. Moore, A. S. Mount, A. M. Rao, E. Alexov, P. C. Ke, *J. Phys. Chem. B* **2006**, *110*, 2475.
[76] M. Uemura, R. A. Joseph, P. L. Steponkus, *Plant Physiol.* **1995**, *109*, 15.
[77] M. S. Webb, B. R. Green, *Biochim. Biophys. Acta* **1991**, *1060*, 133.
[78] F. M. Harris, K. B. Best, J. D. Bell, *Biochim. Biophys. Acta-Biomembranes* **2002**, *1565*, 123.
[79] T. Parasassi, E. K. Krasnowska, L. Bagatolli, E. Gratton, *J. Fluoresc.* **1998**, *8*, 365.
[80] A. Szilagyi, E. Selstam, H. E. Akerlund, *Biochim. Biophys. Acta-Biomembranes* **2008**, *1778*, 348.
[81] P. V Jena, D. Roxbury, T. V Galassi, L. Akkari, C. P. Horoszko, D. B. Iaea, J. Budhathoki-Uprety, N. H. Pipalia, A. S. Haka, J. D. Harvey, *bioRxiv* **2017**, 134999.
[82] J. H. Choi, M. S. Strano, *Appl. Phys. Lett.* **2007**, *90*, 3.
[83] T. Hertel, A. Hagen, V. Talalaev, K. Arnold, F. Hennrich, M. Kappes, S. Rosenthal, J. McBride, H. Ulbricht, E. Flahaut, *Nano Lett.* **2005**, *5*, 511.
[84] G. Bisker, J. Dong, H. D. Park, N. M. Iverson, J. Ahn, J. T. Nelson, M. P. Landry, S. Kruss, M. S. Strano, *Nat. Commun.* **2016**, *7*, 14.
[85] S. Giordani, S. D. Bergin, V. Nicolosi, S. Lebedkin, M. M. Kappes, W. J. Blau, J. N. Coleman, *J. Phys. Chem. B* **2006**, *110*, 15708.
[86] D. A. Heller, E. S. Jeng, T.-K. Yeung, B. M. Martinez, A. E. Moll, J. B. Gastala, M. S. Strano, *Science (80-.).* **2006**, *311*, 508.
[87] A. S. Karakoti, S. Kuchibhatla, K. S. Babu, S. Seal, *J. Phys. Chem. C* **2007**, *111*, 17232.
[88] R. Fettiplace, D. M. Andrews, D. A. Haydon, *J. Membr. Biol.* **1971**, *5*, 277.
[89] U. Zimmermann, G. A. Neil, *Electromanipulation of Cells*, CRC Press, **1996**.
[90] B. Wang, L. Zhang, S. C. Bae, S. Granick, *Proc. Natl. Acad. Sci.* **2008**, *105*, 18171.
[91] M. Kupiainen, E. Falck, S. Ollila, P. Niemelä, A. A. Gurtovenko, M. T. Hyvönen, M. Patra, M. Karttunen, I. Vattulainen, *J. Comput. Theor. Nanosci.* **2005**, *2*, 401.

Tables

Table 1. Parameters Used in LEEP Model

Model parameters	Approximate value	Reference
ε_M	7.0 (protoplast) 2.2 (chloroplast)	[50] [88]
ε_W	80	
γ_0	0.6 mN/m	[89]
Γ	10^{-12} N	[89]
$\Delta\Delta H$	0.05 k_bT	[34,90]
ρ_n	10^{18}	[91]
L	1.1 x 10^{-10} m	[46]
γ_{max}	5 mN/m	[53,54]
Γ_{max}	30 pN	[55,56]

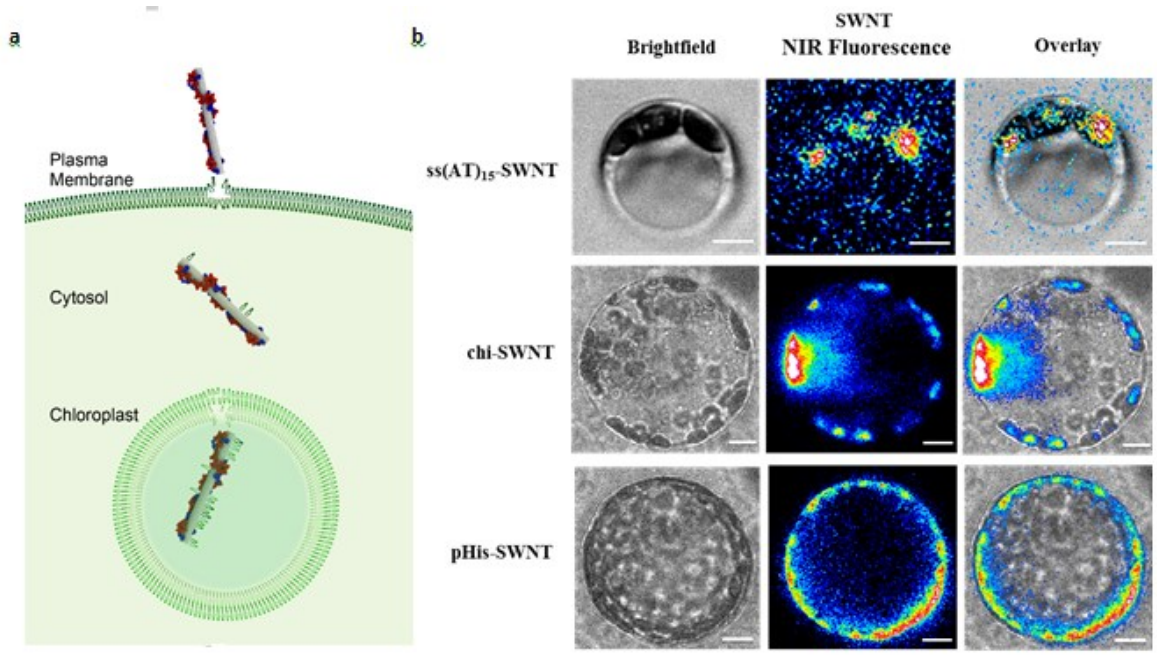

Figure 1. Subcellular localization of nanoparticles within plant mesophyll protoplasts. (a) Schematic illustration of the intracellular fate of nanoparticles. Nanoparticles may traverse past the protoplast membrane passively and localize within the cytosol or traffic past the double lipid bilayers of chloroplasts before being kinetically trapped. (b) Protoplasts incubated with different polymer-wrapped SWNTs with high surface charge, irrespective of the sign of the zeta potential, show high concentration of SWNTs localized in the chloroplasts. Scale bar = 5 μm.

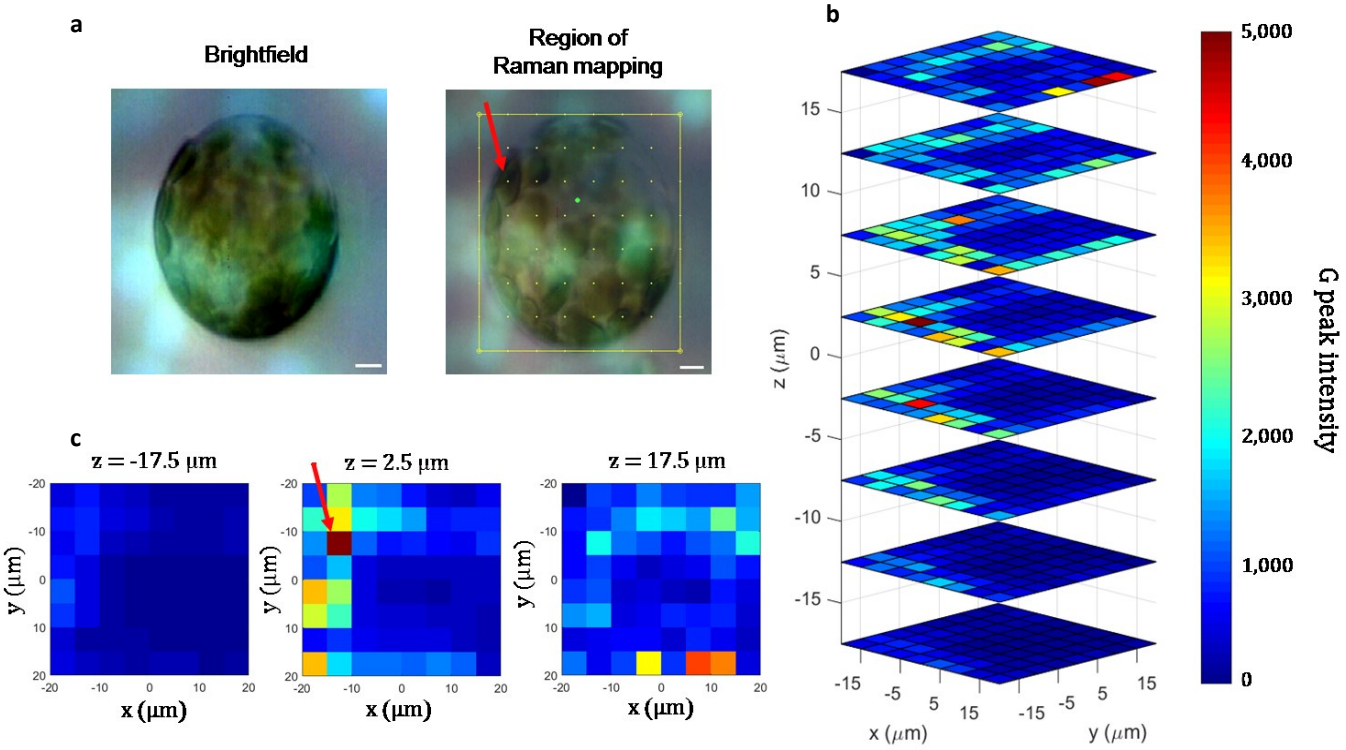

Figure 2. Confocal three-dimensional Raman mapping of the characteristic SWNT G-band to investigate the spatial distribution of ss(AT)$_{15}$-SWNT inside the protoplasts. Confocal Raman spectroscopy can unambiguously distinguish external surface adsorbed SWNTs from those internalized within the protoplast. (a) Brightfield and spatial map showing the location of Raman mapping. Each point of the scanning grid indicates the center of the tiles in the 8x8 mapping region represented in (b) and (c). Scale bar = 5 µm. (b) Z-stack analysis of SWNT Raman mapping in protoplasts with spatial resolution of 5 µm in x and y axis. Values correspond to SWNT G-band intensity (1,580 cm^{-1}) under a laser excitation of 785 nm excitation. (c) The maximum G-band is found within the protoplast and spatial mapping shows the colocalization of SWNTs within the chloroplasts. Red arrow indicates the location of SWNTs which coincide with the position of chloroplasts.

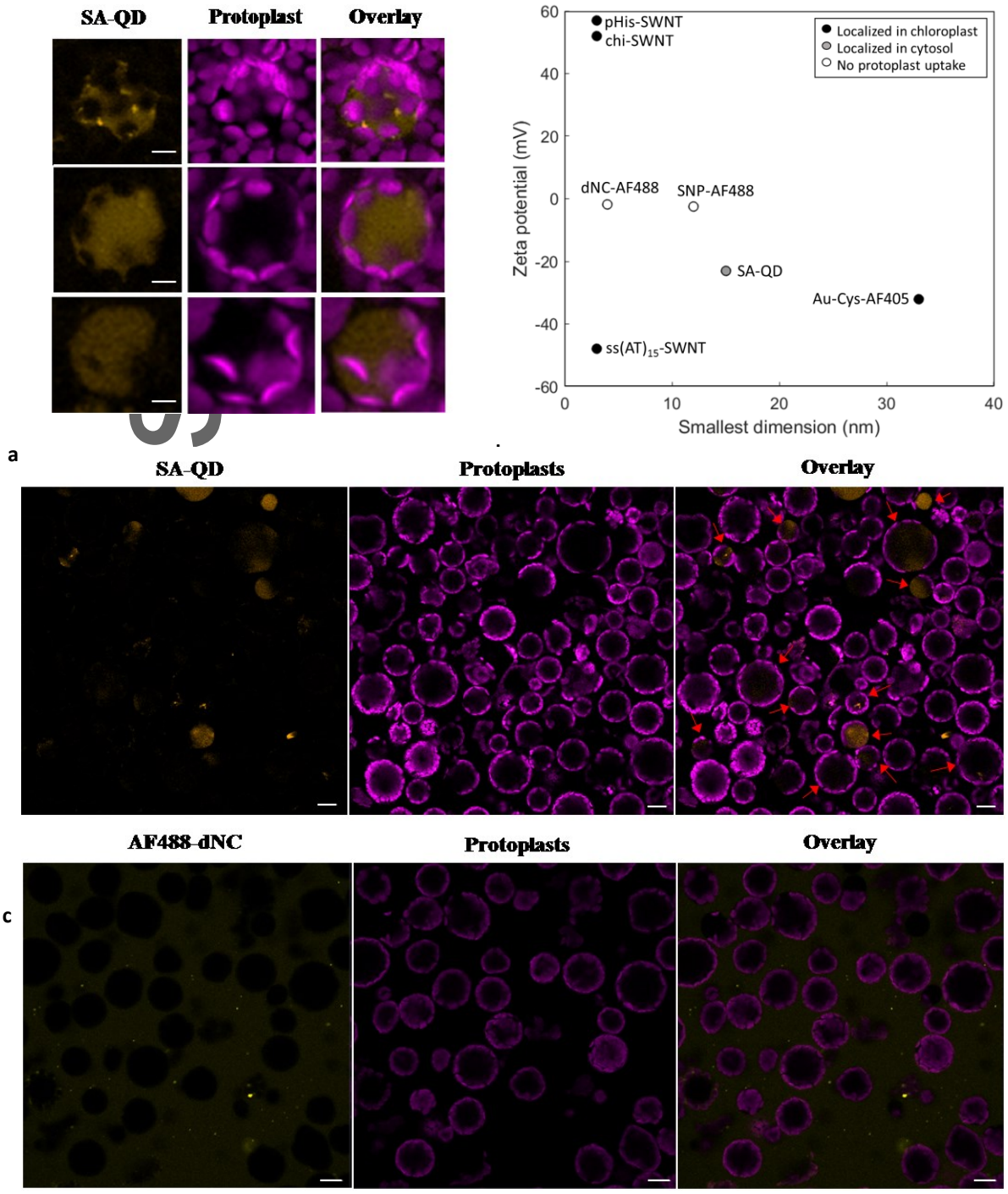

Figure 3. Entry of nanoparticles into protoplasts depends on nanoparticle surface charge and dimension. (a) Confocal images of protoplasts incubated with SA-QD at 4°C for 16 h shows localization of SA-QD within the cytosol of protoplasts as they are unable to penetrate into the

chloroplast interior. Scale bar = 20 µm. (b) Zeta potential and physical dimension of nanoparticles investigated in this study. (c) Confocal micrographs show the heterogeneous uptake distribution among protoplasts for SA-QD, while no internalization was observed for dNC-AF488. Red arrows show viable protoplasts with nanoparticle uptake. Scale bar = 20 µm.

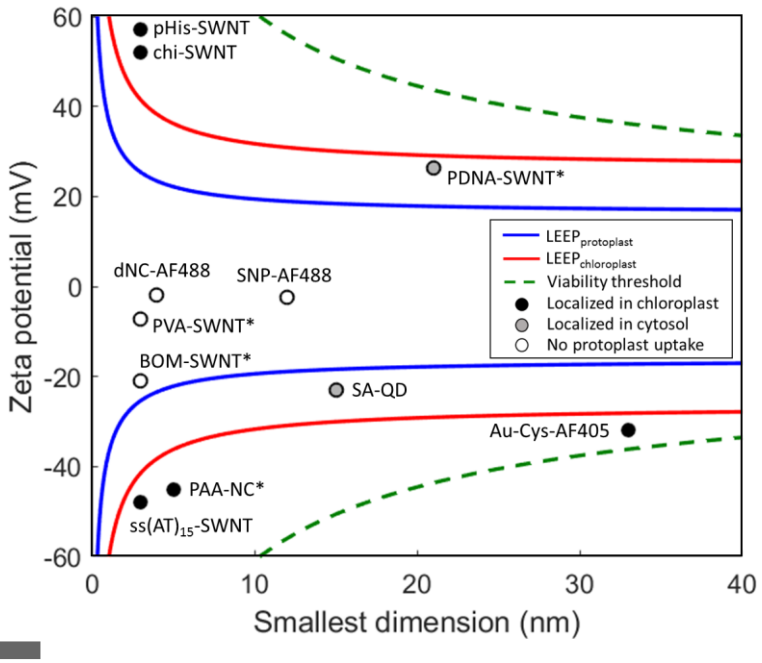

Figure 4. LEEP model explains the entry and distribution of nanoparticles inside protoplasts. LEEP model for protoplasts and chloroplasts are indicated by blue and red lines respectively, while the threshold to maintain protoplast viability is shown by the dashed green lines. The LEEP model can not only explain the experimental observations in this study, but also nanoparticles investigated in previous studies[19,23,57] (denoted by *), which include SWNTs wrapped with polyvinyl alcohol (PVA-SWNT), bombolitin II peptide (BOM-SWNT), polyacrylic acid-nanoceria (PAA-NC) and polyethylenimine-modified SWNT conjugated with plasmid DNA (PDNA-SWNT).

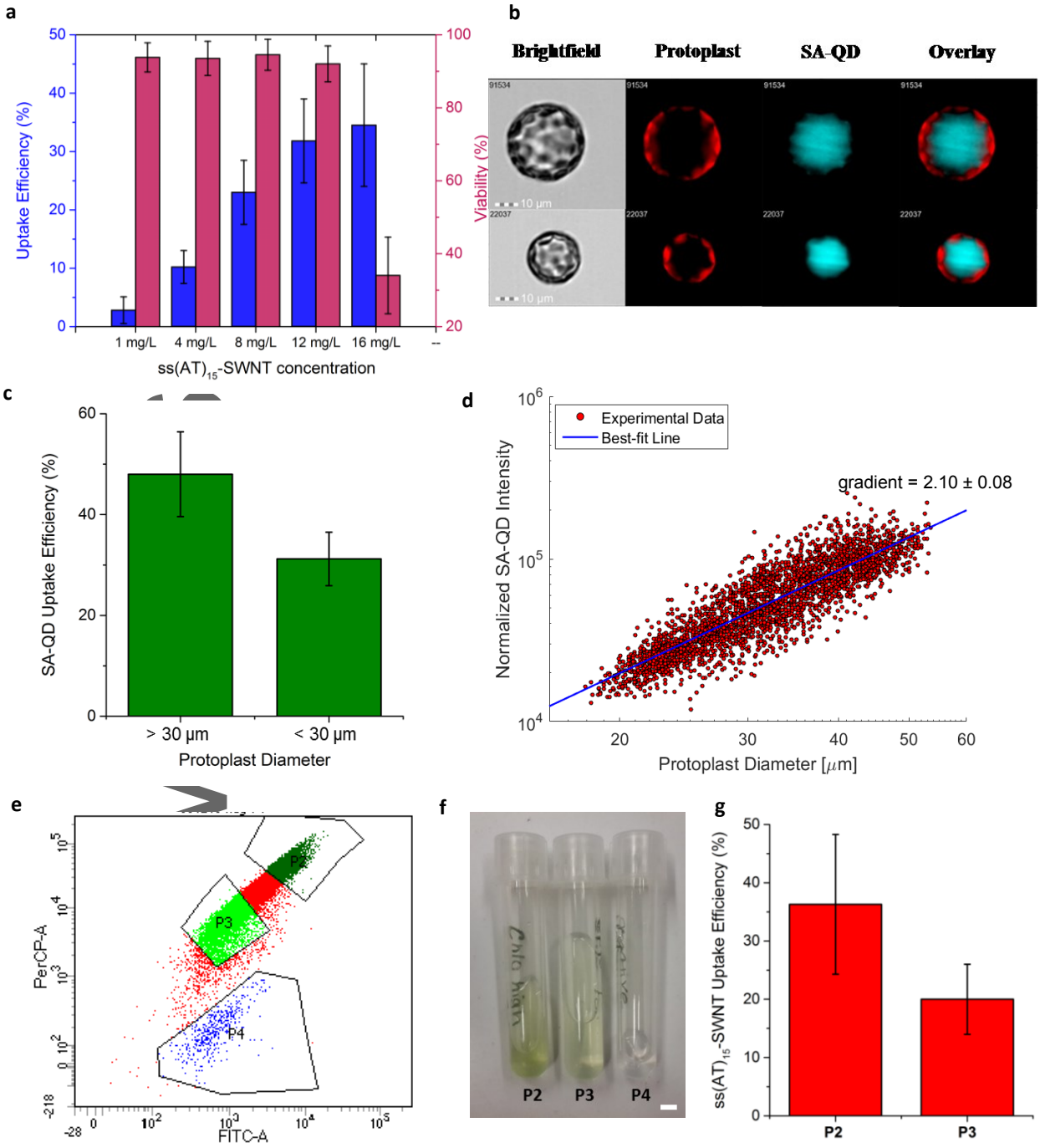

Figure 5. Imaging flow cytometry and fluorescence-activated cell sorting analysis to investigate nanoparticle uptake for sub-populations of protoplasts. (a) Uptake efficiency of ss(AT)$_{15}$-SWNTs into protoplasts and its influence on protoplast viability depend on nanoparticle concentration. Error bars are standard errors of the mean (n = 3). (b) Representative images from imaging flow cytometry which shows the uptake of SA-QD for both large and small protoplasts. Scale bar = 10 µm. (c)

Relative uptake efficiency of nanoparticle into protoplasts as a function of protoplast size. Two-tailed p value is 0.012. (d) Log-log plot of SA-QD channel intensity (normalized by area) against the protoplast diameter. The best-fit line slope of 2.10 indicates that the uptake of SA-QD is correlated with the surface area of the protoplasts. (e) Sub-population of protoplasts sorted via FACS based on their chloroplast content. Gating was determined based on green-red fluorescence. P2 contains the highest chlorophyll content while P3 contains low chlorophyll content. P4 denotes the sub-population that contains cell wall debris with little viable protoplasts. (f) Representative pictures of each protoplast sub-population after cell sorting. Scale bar = 1 cm. (g) Quantitative analysis shows higher uptake efficiency of ss$(AT)_{15}$-SWNT for sub-population of protoplasts with higher chlorophyll content. Two-tailed p value is 0.030. Error bars are standard errors of the mean (n = 3).

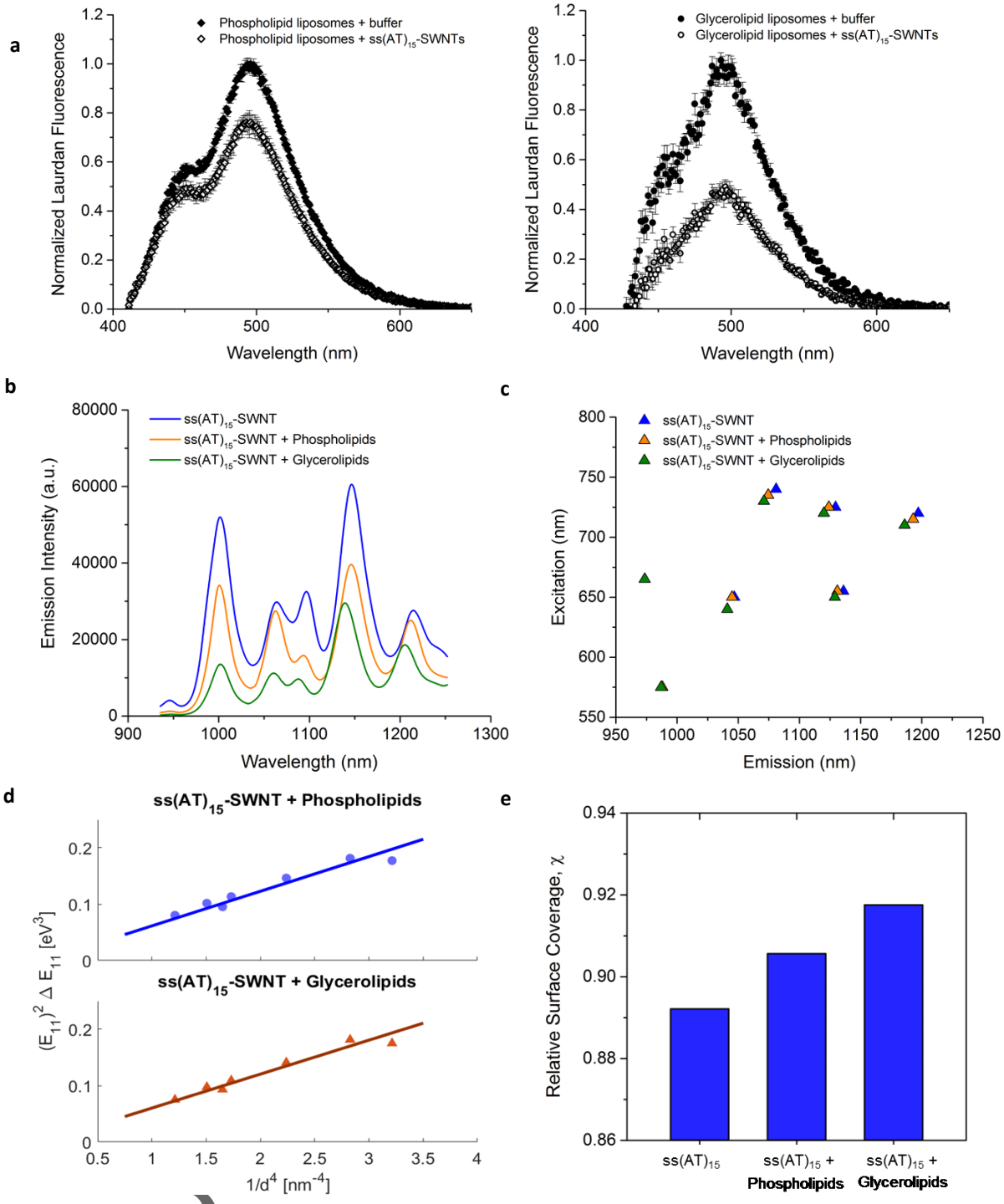

Figure 6. Charged nanoparticles exhibit stronger interaction with glycerolipids than phospholipids. (a) Introduction of ss(AT)$_{15}$-SWNT quenches laurdan fluorescence in DGDG and MGDGG liposomes to a higher extent than in 16:0/18:2-PC liposomes. Error bars represent standard deviations (n = 3).

(b) Incubation of ss$(AT)_{15}$-SWNT with glycerolipid molecules leads to higher intensity attenuation and larger solvatochromic shift than with phospholipid molecules. Sample was excited using 785 nm laser. (c) Profile of center wavelengths of nanotube excitation and emission peaks collected from excitation/emission spectra confirm that glycerolipids induce larger solvatochromic response (blue-shift) than phosopholipids. (d) Solvatochromic shifts of ss$(AT)_{15}$-SWNT with phospholipids and glycerolipids (dots) exhibit linear relationship with SWNT diameter to the power of negative 4 (d^{-4}). (e) The relative surface coverages of pure ss$(AT)_{15}$-SWNT and DNA-lipid complexes calculated from the slopes of linear fitting of (d).

Table of contents entry:

An experimentally-validated lipid exchange envelope penetration (LEEP) model is developed to predict and explain the transport of nanoparticles into protoplast and chloroplast. The specific interactions between nanoparticles and different plant membranes are also investigated to enable targeted delivery of nanoparticles into plant cells without the use of chemical or mechanical aid.

Keywords: plant protoplasts; targeted delivery; zeta potential; single-walled carbon nanotubes; imaging flow cytometry.

T. T. S. Lew, M. H. Wong, Dr. S.Y. Kwak, R. Sinclair, Dr. V. B. Koman, Prof. M. S. Strano

Rational Design Principles for the Transport and Subcellular Distribution of Nanomaterials into Plant Protoplasts